A Wide-Area Situational Awareness Model for Sequential Restoration of Inverter-Dominated Smart Grids

Chaudhry Talha Hassan, Muhammad Shamaas, Tariq Mahmood Jadoon

Department of Electrical Engineering, Lahore University of Management Sciences, Lahore 54792, Pakistan

chaudhry.hassan@lums.edu.pk, muhammad.shamaas@lums.edu.pk, jadoon@lums.edu.pk

Abstract *–After a major blackout, a self-sufficient smart grid can restore healthy nodes by forming microgrids around black start distributed generators (DGs). These microgrids grow gradually over time until all the critical loads are restored. The constellation of faults and radiality constraints determine the load pick-up order and boundaries of microgrids. However, the microgrid restoration optimization model can only approximate the steady-state power network equations. The unpredictable transient response can cause unwanted disturbance to all connected nodes. Hence, the real-time transient results of electrical power flow must be used to enforce dynamic stability after every restoration stage. In this research, measurements from distributed phasor measurement units (PMUs) are used to quantify the disturbance experienced by the loads, generators, and lines. This feedback is used to restrain the restoration algorithm so that the microgrid gets sufficient time to stabilize. The rolling horizon restoration optimization problem is formulated as a mixed-integer second-order cone program (MISOCP). The network traffic for wide-area situational awareness (WASA) is simulated in NS-3, whereas the power system simulation is performed in GridLAB-D. The approach is validated over a modified IEEE-123 node test feeder, and the results are presented to demonstrate the efficacy of the framework for multiple fault scenarios.*

Keywords: Wide-area situational awareness (WASA), mixed-integer second-order cone programming (MISOCP), inverter-based distributed generator (IBDG), energy storage system (ESS)

NOMENCLATURE

Sets

Ω_{BK}	Set of bus blocks.
Ω_{BS}	Set of generators with black start capability.
Ω_G	Set of generators.
Ω_{IBDG}	Set of inverter-based generators.
Ω_L	Set of distribution lines.
Ω_{NBS}	Set of generators without black start capability.
Ω_{NSW}	Set of non-switchable lines.
Ω_{φ}	Set of phases.
Ω_{SG}	Set of synchronous generators.
Ω_{SW}	Set of switchable lines.
Ω_Z	Set of loads.

Indices

bk	Index of bus block.
g	Index of generator.
i, j	Index of bus.
k, l	Index of distribution line.
m	Index of microgrid.
φ	Index of phase.
t	Index of time step.
z	Index of load.

Parameters

α	Multiplier for dynamic stability factor equation.
B_{ij}	Imaginary part of transmission line admittance.
D	Load damping rate
D_P	P-ω and Q-V droop gains.
f_0	Nominal steady state frequency.
f_{max}	Maximum allowable frequency limit.
f_{min}	Minimum allowable frequency limit.
G_{ij}	Real part of transmission line admittance.
H	System inertia.
$I_{l,max}^{line}$	Maximum phase current limit of distribution line l.
I_{θ}	Power factor angle of constant current load.
$J_{i,j}$	$i \times j$ matrix of ones.
M	Big-M number.
$P_{l,\varphi}^{line}$	3×3 Phase matrix of line l.
$P_{g,max}^{gen}$	Maximum output real power limit of generator g.
$P_{l,max}^{line}$	Maximum output real power limit of distribution line l.
P_{θ}	Power factor angle of constant power load.
PLF_l^{line}	Line loss factor for active power.
$Q_{g,max}^{gen}$	Maximum output reactive power limit of generator g.
$Q_{l,max}^{line}$	Maximum output reactive power limit of distribution line l.
QLF_l^{line}	Line loss factor for reactive power.
R_l	3×3 resistance matrix of line l.
$S_{l,max}^{line}$	Maximum output apparent power limit of distribution line l.
$S_{b,max}^{ESS}$	Maximum input apparent power limit of ESS b.
$S_{g,max}^{gen}$	Maximum output apparent power limit of generator g.
S_n	Nominal apparent power rating of ZIP load.
$SOC_{b,max}^{ESS}$	Maximum limit of SOC for ESS b.
$SOC_{b,min}^{ESS}$	Minimum limit of SOC for ESS b.

T	Length of rolling horizon.
$U_{i,max}^{bus}$	Maximum squared voltage magnitude limit of bus i.
$U_{i,min}^{bus}$	Minimum squared voltage magnitude limit of bus i.
V_0	Nominal phase to ground rms bus voltage.
w_i^{load}	Priority weight for load of bus i.
X_l	3×3 Reactance matrix of line l.
Z_l	3×3 Impedance matrix of line l.
Z_θ	Power factor angle of constant impedance load.
Δf^{max}	Limit for maximum allowable frequency deviation.
Δf^{meas}	Measured maximum transient frequency deviation.
ΔI^{max}	Limit for maximum allowable current deviation.
ΔI^{meas}	Measured maximum transient current deviation.
ΔV^{max}	Limit for maximum allowable voltage deviation.
ΔV^{meas}	Measured maximum transient voltage deviation.
Δt	Time step between two restoration stages.
η_b^{ESS}	Charging efficiency of ESS b.

Variables

$DF_{m,t}$	Disturbance factor of microgrid m at stage t.
P_i^{bus}	Real power injection at bus i.
$P_{b,\varphi,t}^{ESS}$	Active power output of ESS b, phase φ at stage t.
$P_{m,t}^{res}$	Limit of maximum restored load for microgrid m at stage t.
$P_{l,\varphi,t}^{line}$	Active power flow of line l, phase φ at stage t.
$P_{l,\varphi,t}^{lineloss}$	Active power loss of line l, phase φ at stage t.
$P_{g,\varphi,t}^{gen}$	Active power output of generator g, phase φ at stage t.
$P_{z,\varphi,t}^{load}$	Active power demand of load z, phase φ at stage t.
Q_i^{bus}	Reactive power injection at bus i.
$Q_{b,\varphi,t}^{ESS}$	Reactive power output of ESS b, phase φ at stage t.
$Q_{l,\varphi,t}^{line}$	Reactive power flow of line l, phase φ at stage t.
$Q_{l,\varphi,t}^{lineloss}$	Reactive power loss of line l, phase φ at stage t.
$Q_{g,\varphi,t}^{gen}$	Reactive power output of generator g, phase φ at stage t.
$Q_{z,\varphi,t}^{load}$	Reactive power demand of load z, phase φ at stage t.
$SOC_{b,\varphi,t}^{ESS}$	SOC of ESS b, phase φ at stage t.
$U_{i,t}^{bus}$	3×1 squared three-phase voltage magnitude matrix of bus i at stage t.
$V_{i,t}^{bus}$	Phase to ground rms voltage of bus i at stage t.
$x_{i,t}^{bus}$	Binary energization status of bus i.
$x_{bk,t}^{busblock}$	Binary energization status of bus block bk.
$x_{b,t}^{charge}$	Binary charging status of ESS b.
$x_{g,t}^{gen}$	Binary energization status of generator g.
$x_{l,t}^{line}$	Binary energization status of line l.
$x_{z,t}^{load}$	Binary energization status of load l.
ΔP_{IBDG}	Increased output from inverter-based generators.
ΔP_L	Total generation loss.
$\Delta P_{m,t}^{res}$	Maximum limit for restored load of microgrid m at stage t.
ΔP_{SG}	Increased output from synchronous generators.
θ_i^{bus}	Angle of voltage at bus i.

I. Introduction

Advancement in smart grid technologies has called for higher reliability of service to consumers. Although faults and outages are inevitable, service must be restored to normal in the event of a blackout. During such an emergency, the generation capacity and energy reserves must be carefully utilized to recover critical loads. An effective method for emergency service restoration is the sectionalization of the power network into microgrids [1]. These autonomous units coordinate all the decisions for self-healing. Hence, power restoration can be achieved in a distributed and decentralized manner [2].

Bulk power distribution networks have limited number of switchable lines and loads [3]. Hence, the network can often be sectioned into large bus blocks [4]. Switching many inductive loads at once can result in severe frequency and voltage oscillations. This makes the service restoration process very hasty and aggressive. Voltage and current spikes can get amplified when they pass through distribution transformers. Such hostility can cause severe damage to inverters and energy storage devices [5].

Modern smart grids can have an extensive range of loads, switches, and auxiliary equipment. Multiple practical limits must be considered for the sequential switching of manual and remote-controlled switches [4]. The operating time of a switch can be impacted by its type, its location [6], and the constraints of the communication channel [7]. Coordination of switches is also important to prevent the overloading of power generators. All the possible changes in network topology must be considered to make feasible microgrids with radial structure and sufficient generation capacity [7].

Microgrid restoration can be very challenging for inverter-dominated smart grids because these networks suffer from poor dynamic stability [8]. Operating multiple inverter-based generators can be difficult if they have dissimilar droop characteristics and ramp limitations. The unpredictable nature of non-linear semiconductor devices makes inverters especially susceptible to damage during electrical overloads, voltage fluctuations, and short-circuit faults [9]. Inverters can face commutation failure or permanent damage if the maximum limits for safe operation are breached [10]. Optimal power exchange must be ensured to prevent the overstressing of IBDGs [2].

The most serious problem with restoring three-phase unbalanced power distribution networks is the overheating of generators due to current unbalance, excessive ramping, frequency drop, and voltage oscillations [11] [12]. To prevent damage to generators, a sufficient spinning reserve must be maintained to compensate for errors in load forecast [1]. The microgrid frequency response rate can be approximated based on the total generation capacity of restored generators [14] [15]. By limiting the ramp rate of synchronous generators, the RoCoF can be reduced to a reasonable value [13] [10] [16]. The health of energy storage systems must also be monitored for inverter-based generators. A strategic charging and discharging strategy must be formulated to maintain SOC within a safe limit [13]. Such approximation methods can effectively constrain the maximum frequency drop by limiting the maximum recovered load in each stage [12]. However, these techniques cannot be applied to inverter-based generators with unbalanced loading [9] [8]. The frequency response of low-inertia inverters is highly unpredictable. Static as well as dynamic constraints for

voltage, current, and frequency must be imposed to prevent damage to sensitive electronic equipment [17] [18] [8] [3] [5].

Power flow analysis is a useful tool for a variety of power system applications. Several models and algorithms have been developed for optimal power flow analysis. This convex problem can be simplified through several approximations and relaxations. Constant current and constant impedance loads can be represented using linearized power flow models [11]. Shunt capacitors, voltage regulators, and distribution transformers can also be represented using linear constraints. Overloading of transformers and transmission lines can be prevented using quadratic or approximate polygon-based linearized constraints [13] [11]. The problem of power flow in an unbalanced multi-phase radial network has been solved using semi-definite programming. Conic and semi-definite optimization is useful for transmission system planning and distribution system reconfiguration. Mixed-integer models with quadratic, conic, and semi-definite optimization have been successful for power loss analysis [15]. Load flow problems in radially distributed networks have been solved by convex or conic optimization programs [15]. Although complex optimization problems can accurately model the steady-state behavior of these power system elements, their transient behavior cannot be predicted. An active wide-area monitoring system is required to ensure safe operation during switching operations and power shuffling [3].

A centralized approach to load restoration considers it as a classical optimization problem to maximize critical load pickup while incorporating power system constraints. The restoration process can be optimized through various techniques. The most powerful methods for solving this optimization problem include mixed-integer linear programming, dynamic programming, multi-agent systems, and heuristic algorithms [19]. Although it can lead to suboptimal solutions, linear programming has the lowest computation cost and the highest rate of convergence compared to all other methods [4]. For fault restoration of smart grids involving renewable energy sources, energy generation cannot be accurately forecasted [19] [15] [2]. Load diversity can also be highly unpredictable after a blackout [13] [7]. Hence, a combination of stochastic optimization and mixed-integer linear programming is preferred. This can provide reliable solutions with a high convergence rate and computation speed [13] [19] [18] [2] [20].

The role of a synchronous generator as a black-start capable DG has not been studied in detail for service restoration problems. Besides improving electrical stability, high-inertia diesel generators can act as reliable power sources, unlike renewable energy generators [21]. There are new opportunities to consider synchronous generators or backup generators (BUGs) as a source of black start capability [10]. Ramp constraints, inertial capacities of prime-movers, and generator excitation characteristics are important for modelling their operation. By incorporating these constraints, the utility of BUGs can be increased to harness power and improve microgrid stability.

Standardization of smart grid communication technologies has offered new opportunities for improving protection and control of green smart grids. With the increasing installation of remote-controlled smart switches, tie-lines, isolators, and distributed energy resources, there is a growing need for improving this communication layer in cyber-physical distribution systems. Power quality monitoring modules integrated with high-frequency transceivers allow real-time monitoring of transient fault records with millisecond precision. Active management of smart grids is now possible with improved processing power and fast networking solutions.

II. MOTIVATION AND CONTRIBUTION

Reconfiguration of an inverter-dominated distribution system is a complex combinatorial problem due to non-linear power flow equations and the unpredictable generation of renewable energy sources. A highly complicated optimization scheme is needed to incorporate all the intricacies of the analog and digital components. The optimization model can only approximate the electrical power network equations. Hence, the results of electrical power flow must be used to reinforce dynamic stability after every restoration stage.

An intelligent control system must be well informed about the situation of all the constituent subsystems. The control commands must be based on real-time data obtained from distributed field devices. In short, an active management system is needed to sense and optimally control all the distributed subsystems. The proposed model is shown in Figure 1.
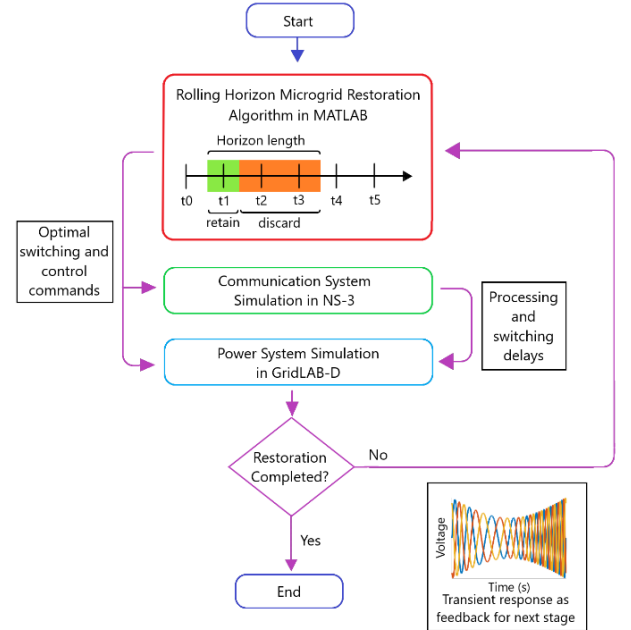

Figure 1: Three-level sequential microgrid restoration model.

In this research, the restoration optimization problem is formulated as a mixed-integer second-order cone program. The restoration commands were implemented over a distributed control framework. All the loads, generators, and switches could be controlled remotely. The different subsystems used two-way negotiations to exchange information and control signals across the network.

Based on the communication requirements, network traffic was simulated in NS-3 to determine the latencies and QoS of the network. The resulting reconfiguration commands and inter-switch operating delays were finally simulated in GridLAB-D to determine the transient response.

This work makes an important contribution to the cyber-physical implementation of a resilient distribution system. For effective sequential microgrid restoration, the effects of past

decisions must impact the formulation of the next optimization stage. After each restoration stage, a scan of the entire network was acquired to judge the electrical stability of the recovered region. Further load restoration was delayed if the network qualified as unstable. The real-time feedback allowed the central controller to carry out time-sensitive optimization tasks. The measurements of distributed PMUs provided feedback for the next stage of the rolling horizon restoration optimization problem.

This research aims to achieve the following goals:

1. Develop a decentralized control architecture for the restoration of inverter-dominated microgrids. The utility operator was provided with all the relevant information for controlling distributed generators, reconfiguring the distribution network, and forecasting load demand. The autonomous central controller performed MISOCP optimization for all supervisory tasks. Besides routine tasks like controlling distributed generators, demand response, and Volt-Var regulation, it also performed network reconfiguration. Based on the restoration solution, it distributed control commands to the different microgrid controllers. These autonomous controllers were responsible for coordinating the operation of distributed loads, switches and generators.

2. Execute information exchange to coordinate the control and protection of microgrids during sequential service restoration. The microgrid controller was responsible for monitoring all the widespread loads, lines and generators. It aggregated the status information and distributed the control commands for all the subsystems. The hierarchical structure for data exchange was implemented using a fast and reliable communication system in NS-3.

3. Quantify the aggression afflicted during each microgrid restoration stage to provide feedback for the microgrid protection system. After every restoration stage, the transient fault records of the GridLAB-D simulation were analyzed to quantify the disturbance experienced by the microgrid. The maximum deviations in load voltages, line currents, and generator frequencies were used to calculate the microgrid disturbance factor. A rolling horizon optimization framework was implemented to modulate the load restoration limit based on the microgrid disturbance factor. This factor restrained the sequential restoration algorithm so that the next stage could be improved.

III. FORMULATION OF OPTIMIZATION PROBLEM

A MISOCP optimization problem was formulated for the restoration of the damaged IEEE-123 bus system shown in Figure 2. The modified network contained three-phase diesel generators, PV generators, and EV charging stations. Each generator had a rating of 300kW and a ramp limit of 50 kW/s.

The service restoration system executed a self-healing algorithm. The initial decision for network reconfiguration was based on the fault location input. The unhealthy region was isolated immediately. Afterward, iterative microgrid formation started.

The healthy bus blocks were enumerated and grouped based on geographic proximity. The bus blocks that could be connected via switchable lines were assigned a microgrid. This determined the boundaries of the microgrids.

For each microgrid, a root node was assigned, which would be solely responsible for exchanging the status and control information with the utility operation center. The high-rank node had a diesel generator with black start capability. An iterative depth-first search algorithm was used to rank bus blocks in order of energization. The bus blocks closer to the root node would be energized earlier.
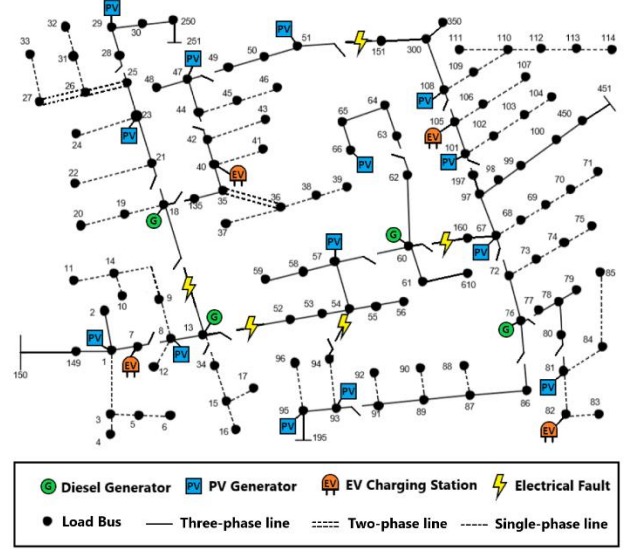

Figure 2: Damaged IEEE 123 bus distribution network

Operational planning determined the optimal switching pattern for demand response management, network reconfiguration, fault level management, and Volt-Var control. Load forecast, unit availability, and energy storage capacity were used for controlling generation.

The objective function (1) aims to maximize the total recovered loads over a rolling horizon $[t, t + T]$. The priorities of the bus blocks were assigned randomly. Each load had the same weight as its bus block.

$$\max \sum_{t \in [t, t+T]} \sum_{z \in \Omega_Z} \sum_{\varphi \in \Omega_\varphi} \left(w_z^{load} x_{z,t}^{load} P_{z,\varphi,t}^{load} \right) \qquad (1)$$

1. Nodal power balance constraints: Constraints (2)-(3) define the nodal balance of active and reactive power for each phase. The linearized DistFlow equations were used to approximate the electrical power flow [2]. They state that the generated power must be equal to the sum of load demand, transmitted power, and line losses.

$$\forall i \forall \varphi \forall t \left[\sum_{l \in \Omega_i} (P_{l,\varphi,t}^{line} + P_{l,\varphi,t}^{lineloss}) + x_{i,t}^{load} P_{i,\varphi,t}^{load} - P_{i,\varphi,t}^{ESS} = P_{i,\varphi,t}^{gen} \right] \qquad (2)$$

$$\forall i \forall \varphi \forall t \left[\sum_{l \in \Omega_i} (Q_{l,\varphi,t}^{line} + Q_{l,\varphi,t}^{lineloss}) + x_{i,t}^{load} Q_{i,\varphi,t}^{load} - Q_{i,\varphi,t}^{ESS} = Q_{i,\varphi,t}^{gen} \right] \qquad (3)$$

2. Transmission line constraints: Constraints (4)-(7) define the limits for transmission line active power losses and reactive power losses. The line losses were calculated using the average loss factor and the apparent power flow of the line. The line loss factor was estimated by assuming a maximum voltage drop of 5% across the line.

$$PLF_l^{line} \approx \frac{P_{l,max}^{lineloss}}{S_{l,max}^{line}} = \frac{R_l I_{l,max}^{line\ 2}}{V_0 I_{l,max}^{line}} = \frac{0.05 R_l}{\sqrt{R_l^2 + X_l^2}}; \quad I_{l,max}^{line} \approx \frac{0.05 V_0}{\sqrt{R_l^2 + X_l^2}} \quad (4)$$

$$QLF_l^{line} \approx \frac{Q_{l,max}^{lineloss}}{S_{l,max}^{line}} = \frac{X_l I_{l,max}^{line\ 2}}{V_0 I_{l,max}^{line}} = \frac{0.05 X_l}{\sqrt{R_l^2 + X_l^2}}; \quad I_{l,max}^{line} \approx \frac{0.05 V_0}{\sqrt{R_l^2 + X_l^2}} \quad (5)$$

$$\forall l \epsilon \Omega_L \forall t \left[P_{l,t}^{lineloss} \geq PLF_l^{line} \left\| \begin{matrix} P_{l,\varphi,t}^{line} \\ Q_{l,\varphi,t}^{line} \end{matrix} \right\|_2 \right] \quad (6)$$

$$\forall l \epsilon \Omega_L \forall t \left[Q_{l,t}^{lineloss} \geq QLF_l^{line} \left\| \begin{matrix} P_{l,\varphi,t}^{line} \\ Q_{l,\varphi,t}^{line} \end{matrix} \right\|_2 \right] \quad (7)$$

Constraint (8) defines the transmission line's active and reactive power flow limits. Constraints (9)-(10) state the conditions for the energization of switchable lines. Constraint (11) implies that non-switchable lines are automatically energized whenever the corresponding bus is energized.

$$\forall l \forall \varphi \forall t \left[\left\| \begin{matrix} P_{l,\varphi,t}^{line} \\ Q_{l,\varphi,t}^{line} \end{matrix} \right\|_2 \leq x_{l,t}^{line} S_{l,max}^{line} \right] \quad (8)$$

$$\forall ij, l \epsilon \Omega_{SW} \forall t \left[x_{l,t}^{line} \leq x_{i,t}^{bus} \wedge x_{l,t}^{line} \leq x_{j,t}^{bus} \right] \quad (9)$$

$$\forall ij, l \epsilon \Omega_{SW} \forall t \epsilon [2, \infty) \left[x_{l,t}^{line} \geq x_{l,t-1}^{line} \right] \quad (10)$$

$$\forall ij, l \epsilon \Omega_{NSW} \forall t \left[x_{l,t}^{line} = x_{i,t}^{bus} \wedge x_{l,t}^{line} = x_{j,t}^{bus} \right] \quad (11)$$

3. Generation constraints: Constraints (12)-(13) define the active and reactive power generation limits for generators. Constraints (14)-(18) define the operational limits for charging and discharging of energy storage systems. Constraints (19)–(20) state that a generator without black start capability can only be started if its associated bus is energized, and it cannot be turned off afterwards. Constraints (21)-(22) define the output active and reactive power ramp rates for the distributed generators (PV inverters, PHEV inverters, and diesel generators).

$$\forall g \forall \varphi \forall t \left[\left\| \begin{matrix} P_{g,\varphi,t}^{gen} \\ Q_{g,\varphi,t}^{gen} \end{matrix} \right\|_2 \leq x_{g,t}^{gen} S_{g,max}^{gen} \right] \quad (12)$$

$$\forall g \forall \varphi \forall t \left[P_{g,\varphi,t}^{gen} \geq 0 \wedge Q_{g,\varphi,t}^{gen} \geq 0 \right] \quad (13)$$

$$\forall b \forall \varphi \forall t \left[\left\| \begin{matrix} P_{b,\varphi,t}^{ESS} \\ Q_{b,\varphi,t}^{ESS} \end{matrix} \right\|_2 \leq x_{b,t}^{charge} S_{b,max}^{ESS} \right] \quad (14)$$

$$\forall g \forall \varphi \forall t [x_{g,t}^{charge} + x_{g,t}^{gen} = 1] \quad (15)$$

$$\forall b \forall \varphi \forall t \left[P_{b,\varphi,t}^{ESS} \leq 0 \wedge Q_{b,\varphi,t}^{ESS} \leq 0 \right] \quad (16)$$

$$\forall b \forall \varphi \forall t \left[SOC_{b,\varphi,t}^{ESS} \geq SOC_{b,min}^{ESS} \wedge SOC_{b,\varphi,t}^{ESS} \leq SOC_{b,max}^{ESS} \right] \quad (17)$$

$$\forall b \forall \varphi \forall t \left[SOC_{b,\varphi,t}^{ESS} = SOC_{b,\varphi,t-1}^{ESS} + \eta_b^{ESS} \Delta t \left(P_{b,\varphi,t}^{ESS} - P_{b,\varphi,t}^{gen} + Q_{b,\varphi,t}^{ESS} - Q_{b,\varphi,t}^{gen} \right) \right] \quad (18)$$

$$\forall g \epsilon \Omega_{NBS} \forall t \left[x_{g,t}^{gen} \leq x_{g,t}^{bus} \right] \quad (19)$$

$$\forall g \epsilon \Omega_{NBS} \forall t \epsilon [2, \infty) \left[x_{g,t}^{gen} \geq x_{g,t-1}^{gen} \right] \quad (20)$$

$$\forall g \forall t \epsilon [2, \infty) \left[-\Delta P_{g,max}^{gen} \leq P_{g,t}^{gen} - P_{g,t-1}^{gen} \leq \Delta P_{g,max}^{gen} \right] \quad (21)$$

$$\forall g \forall t \epsilon [2, \infty) \left[-\Delta Q_{g,max}^{gen} \leq Q_{g,t}^{gen} - Q_{g,t-1}^{gen} \leq \Delta Q_{g,max}^{gen} \right] \quad (22)$$

4. Load constraints: Constraint (23) states that a load is energized whenever its corresponding bus has been energized. Constraint (24) states that once a load has started operation, it cannot be stopped.

$$\forall i \forall t \left[x_{i,t}^{load} = x_{i,t}^{bus} \right] \quad (23)$$

$$\forall i \forall t \epsilon [2, \infty) \left[x_{i,t}^{load} \geq x_{i,t-1}^{load} \right] \quad (24)$$

5. Nodal voltage constraints: Constraints (25)-(26) define the limits for the voltage difference between the end nodes of a transmission line. The Big-M notation is used to ensure that these constraints are active only when the line is energized. Constraint (27) ensures that the bus voltage is constrained within predefined limits.

$$\forall ij, l \epsilon \Omega_L \forall \varphi \forall t \left[U_{i,\varphi,t}^{bus} - U_{j,\varphi,t}^{bus} \geq 2 \left(R_l P_{l,\varphi,t}^{line} + X_l Q_{l,\varphi,t}^{line} \right) + \left(x_{l,t}^{line} + P_{l,\varphi}^{line} - 2 \right) M \right] \quad (25)$$

$$\forall ij, l \epsilon \Omega_L \forall \varphi \forall t \left[U_{i,\varphi,t}^{bus} - U_{j,\varphi,t}^{bus} \leq 2 \left(R_l P_{l,\varphi,t}^{line} + X_l Q_{l,\varphi,t}^{line} \right) + \left(2 - x_{l,t}^{line} - P_{l,\varphi}^{line} \right) M \right] \quad (26)$$

$$\forall i \forall \varphi \forall t \left[x_{i,t} U_{i,min}^{bus} \leq U_{i,\varphi,t}^{bus} \leq x_{i,t} U_{i,max}^{bus} \right] \quad (27)$$

6. Bus block switching: The healthy bus blocks were enumerated and grouped based on geographic proximity. The reduced network contained a set of bus blocks Ω_{BK} that were connected by a set of switchable lines:

$$\Omega_{SW} := \{(k, l) \mid k \epsilon \Omega_{BK} \wedge l \epsilon \Omega_{BK} \wedge k \neq l\} \quad (28)$$

The reduced IEEE-123 bus system is shown in Figure 3. Constraint (29) ensures that all the buses in a bus block get energized simultaneously. Constraint (30) ensures that a switchable line cannot be closed if both of its end blocks are already energized. This is required to maintain radial tree topology during microgrid restoration. Constraint (31) states that a bus block can only be switched on by one of the connected switchable lines. Constraint (32) makes sure that at least one connected switchable line is energized before the energization of the bus block. Finally, constraint (33) implies that a switchable line can be energized only if at least one of the connected bus blocks is already energized.

$$\forall i \epsilon \Omega_{bk} \forall t \left[x_{i,t}^{bus} = x_{bk,t}^{busblock} \right] \quad (29)$$

$$\forall k, ij \epsilon \Omega_{sw} \forall t \epsilon [2, \infty) \left[\left(x_{i,t}^{busblock} - x_{i,t-1}^{busblock} \right) + \left(x_{j,t}^{busblock} - x_{j,t-1}^{busblock} \right) \geq \left(x_{k,t}^{line} - x_{k,t-1}^{line} \right) \right] \quad (30)$$

$$\forall k, ij \epsilon \Omega_{sw} \forall t \epsilon [2, \infty) \ [\textstyle\sum_{ki\epsilon\Omega_{sw}}\left(P_{ki,\varphi,t}^{line} - P_{ki,\varphi,t-1}^{line}\right) +$$
$$\textstyle\sum_{ij\epsilon\Omega_{sw}}\left(P_{ij,\varphi,t}^{line} - P_{ij,\varphi,t-1}^{line}\right) \leq 1 + x_{i,t-1}^{busblock} M] \quad (31)$$

$$\forall k, ij \epsilon \Omega_{sw} \forall t \epsilon [2, \infty) \ [x_{i,t-1}^{busblock} \leq \textstyle\sum_{ki \, \epsilon \, \Omega_i} x_{ki,t}^{line} +$$
$$\textstyle\sum_{ij \, \epsilon \, \Omega_i} x_{ij,t}^{line}] \quad (32)$$

$$\forall k, ij \epsilon \Omega_{sw} \forall t \epsilon [2, \infty) \ [x_{ij,t}^{line} \leq x_{i,t-1}^{busblock} + x_{j,t-1}^{busblock}] \quad (33)$$
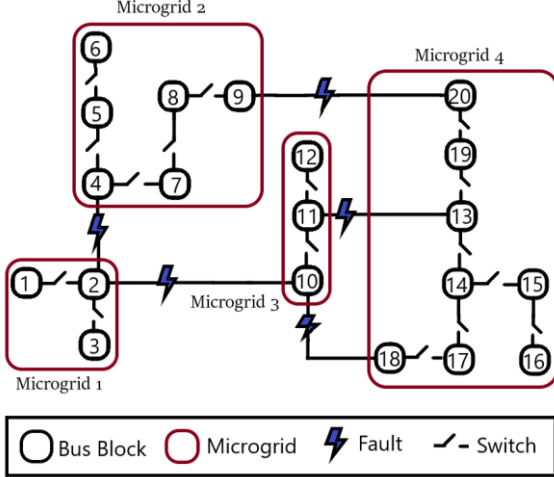
Figure 3: Reduced IEEE-123 bus power network showing bus blocks and microgrids.

7. Dynamic constraints: After a restoration stage was executed, the maximum values for nodal frequency deviation, nodal voltage deviation, and line current deviation were recorded. These values were translated into a numerical parameter for expressing the state of the microgrid. Equation (34) presents the formula for calculating this microgrid disturbance factor. This factor was used to restrain the amount of restored load in the next stage, as expressed in (35)-(36). The maximum nodal voltage deviation and line current deviation of each phase was incorporated to discourage unbalanced loading of the lines and generators.

$$DF_{m,t} = \frac{1}{7}[\textstyle\sum_{i\epsilon\Omega_m} \frac{1}{N_i}\left(\frac{\Delta f_{i,t}^{meas}}{\Delta f^{max}} + \frac{\Delta V_{i,\varphi_A,t}^{meas} + \Delta V_{i,\varphi_B,t}^{meas} + \Delta V_{i,\varphi_C,t}^{meas}}{\Delta V^{max}}\right) +$$
$$\textstyle\sum_{l\epsilon\Omega_m} \frac{1}{N_l}\left(\frac{\Delta I_{l,\varphi_A,t}^{meas} + \Delta I_{l,\varphi_B,t}^{meas} + \Delta I_{l,\varphi_C,t}^{meas}}{\Delta I^{max}}\right)] \quad (34)$$

$$\forall m \forall t \epsilon [2, \infty)[\Delta P_{m,t}^{res} = \Delta P_{m,t-1}^{res} + \alpha(1 - DF_{m,t-1})] \quad (35)$$

$$\forall m \forall t \epsilon [2, \infty)[0 \leq P_{m,t}^{res} \leq P_{m,t-1}^{res} + \Delta P_{m,t}^{res}] \quad (36)$$

IV. COMMUNICATION SYSTEM

A three-level communication network was designed in NS-3 to simulate the coordination between the utility operation center, microgrid controllers, and Intelligent Electronic Devices (IEDs) like phasor measurement units. The complete system is shown in Figure 4.

The Wide Area Network provided remote access of microgrids to the central management system via long-range,

high-capacity WiMAX links. NS-3 provides a realistic implementation of the IEEE-802.16 standard using Wireless MAN-OFDM physical layer, uplink and downlink schedulers, IP packet classifier for the convergence sub-layer, and support for multicast traffic [24]. A base station was installed to serve the subscriber stations installed at the central controller and the microgrid controller nodes. The point-to-multipoint telecommunication network enabled pervasive control of the entire distribution system for time-sensitive tasks like maintaining electrical stability.
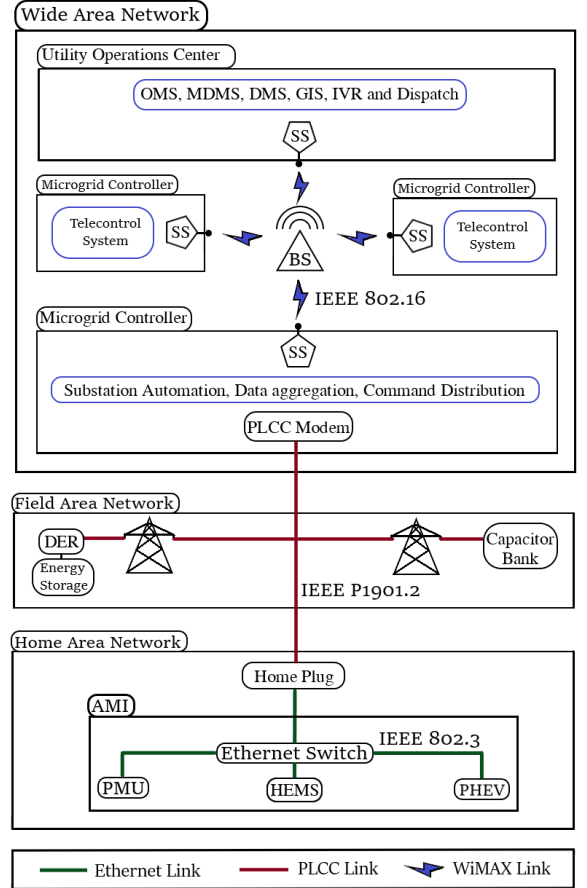

Figure 4: Three-tier communication system for wide area situational awareness model.

Existing power lines were used to transmit control and status signals across the Field Area Network. Each power line communication device was supplemented with a data concentrator for communication with the widespread IEDs. Distributed generators were controlled via programmable logic controllers integrated with SCADA modems. The transmission line channels also conveyed switching commands for capacitor banks, load controllers, and circuit breakers. To ensure dynamic stability throughout the restoration, status signals from all the nodes were relayed periodically to the central controller.

The Home Area Network connected load controllers and sensors via an Ethernet-based AMI. This enabled coordination of a large number of distributed IEDs. These devices continuously collected information from power meters, transducers, and field components for supervision. For fast and reliable communication, the IPv4 protocol was implemented in the network layer, and the UDP protocol was implemented in the transport layer. The IEDs were complemented with data

concentrators for integration; and remote terminal units for communication channel interfacing. The network interface module implemented distributed network protocols for physical interface conversion. The pervasive communication system enabled continuous scanning of operational data for greater control and flexibility. However, the extensive monitoring required enhanced communication channel utilization. The repeated synchronization also introduced substantial computation overhead.

10 Mbps Ethernet links were installed for the Home Area Network, and 2 Mbps links were used for power line carrier communication. Three different WiMAX uplink schedulers were supported in NS-3: the priority based First Come First Serve scheduler (FCFS), the Migration Based Quality of Service scheduler (MBQoS), and the Real Time Polling Service scheduler (RTPS) [24]. The schedulers were compared by simulating desired data traffic and plotting the results of Traffic Control Helper. Figure 5 shows the throughput of the three WiMAX uplink schedulers for different loads.
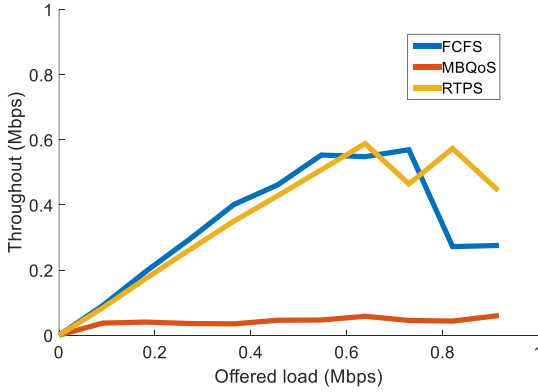
Figure 5: Comparison of throughput of three WiMAX schedulers for Best Effort (BE) service.

Five different service flows were supported, including Unsolicited Grant Service (UGS), Real-Time Polling Service (rtPS), Non-Real Time Polling Service (nrtPS), and Best Effort Service (BE). The priority of the service flows is UGS > rtPS > nrtPS > BE. Special management messages were used for bandwidth management, service flow control, and monitoring of QoS parameters [24]. The different connections were compared by simulating an average data traffic of 0.1 Mbps. The performance of one base station for different WiMAX uplink schedulers and service flows is shown in Figure 6.
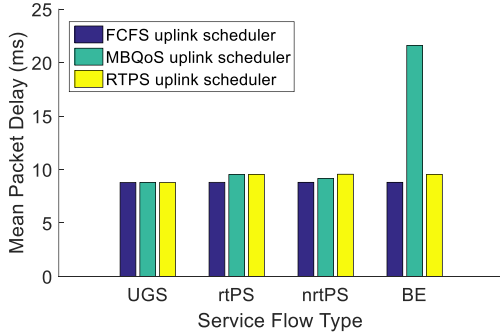

Figure 6: Comparison of mean packet delay for different WiMAX uplink schedulers and service flows.

UGS service flow had the lowest mean packet delay for each uplink scheduler. The most efficient uplink scheduler was FCFS. It performed equally well for all four types of service

flows. Hence, UGS connections with the FCFS uplink scheduler were most suitable for time-sensitive tasks like real-time wide-area situational monitoring.

V. POWER SYSTEM SIMULATION

The IEEE 123-bus modified feeder [23] was simulated in GridLAB-D to verify the MISOCP optimization results. The simulated system was approximated by quadratic approximations in the optimization problem. As expected, the optimization problem could not predict the transient response of power system elements. The discrete-time simulation was used to monitor the dynamics of the inverter-dominated smart grid for the rolling horizon sequential power restoration.

The simulator used the Newton-Raphson method to iteratively solve the power flow equations (37)-(39) until the solution converged [22].

$$\Delta P_i = -P_i + \sum_{j=1}^{N} |V_i||V_j|[G_{ij}cos\theta_{ij} + B_{ij}sin\theta_{ij}] \qquad (37)$$

$$\Delta Q_i = -Q_i + \sum_{j=1}^{N} |V_i||V_j|[G_{ij}sin\theta_{ij} + B_{ij}cos\theta_{ij}] \qquad (38)$$

$$\begin{bmatrix} \Delta\theta \\ |\Delta V| \end{bmatrix} = -\begin{bmatrix} \delta\Delta P/\delta\theta & \delta\Delta P/\delta|V| \\ \delta\Delta Q/\delta\theta & \delta\Delta Q/\delta|V| \end{bmatrix}^{-1} \begin{bmatrix} \Delta P \\ \Delta Q \end{bmatrix} \qquad (39)$$

The optimization problem assumed all the loads to be constant power loads. However, three different types of loads were modelled in GridLAB-D: constant impedance loads, constant current loads, and constant power loads. Their power flow equations are given in (40), (41), and (42) respectively [22].

$$P_i = \frac{|V_i|^2}{|V_0|^2} S_n cos Z_\theta; \; Q_i = \frac{|V_i|^2}{|V_0|^2} S_n sin Z_\theta \qquad (40)$$

$$P_i = \frac{|V_i|}{|V_0|} S_n cos I_\theta; \; Q_i = \frac{|V_i|}{|V_0|} S_n sin I_\theta \qquad (41)$$

$$P_i = S_n cos P_\theta; \; Q_i = S_n sin P_\theta \qquad (42)$$

The transmission lines were simulated using actual parameters for the IEEE-123 bus model. The lumped parameter pi-line model (43) was used to simulate the energization of overhead lines and cables in GridLAB-D [22].

$$\begin{bmatrix} V_a \\ V_b \\ V_c \end{bmatrix}_j = \begin{bmatrix} V_a \\ V_b \\ V_c \end{bmatrix}_i + \begin{bmatrix} Z_{aa} & Z_{ab} & Z_{ac} \\ Z_{ba} & Z_{bb} & Z_{bc} \\ Z_{ca} & Z_{cb} & Z_{cc} \end{bmatrix} \begin{bmatrix} I_a \\ I_b \\ I_c \end{bmatrix} \qquad (43)$$

The optimization problem considered diesel generators as a variable PQ source without any consideration for their dynamic behavior. The GridLAB-D implementation of the diesel generator governor is shown in Figure 7. It incorporated the dynamic behavior of the electromechanical control system for a realistic implementation of a synchronous generator [22].
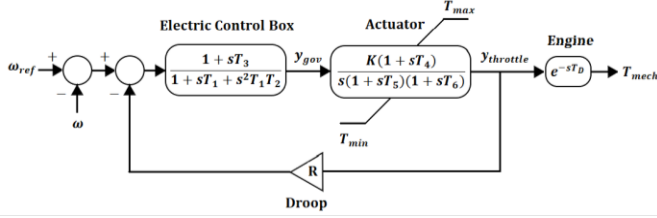
Figure 7: Diagram of GGOV diesel generator governor.

Similarly, the optimization problem considered the inverter as a variable PQ source without considering its dynamic behavior. The GridLAB-D implementation included a more sophisticated model with frequency and voltage droop control. The diagram of the droop mode voltage source inverter [9] [22] is shown in Figure 8.
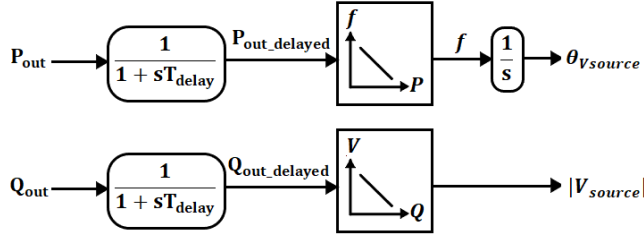

Figure 8: Diagram of droop mode voltage source inverter.

The solar panel was modeled as a controllable current source in GridLAB-D. The output current was effected by the light intensity, temperature and voltage parameters [22].

The incorporation of complex dynamic models made the simulation much more realistic compared to the optimization problem. The overall microgrid frequency response [10] can be approximated by the first-order swing equation (44).

$$\frac{d\Delta f(t)}{dt} = \frac{1}{2H}\left(\Delta P_{SG}(t) + \Delta P_{IBDG}(t) - \Delta P_L(t) - D.\Delta f(t)\right) \quad (44)$$

VI.   SIMULATION RESULTS

The simulation of the cyber-physical smart grid was carried out in three steps. First, the MISOCP optimization problem was solved to determine the optimal switching and control commands. Then, the NS-3 communication system simulation was run to determine the delays in the transmission of information to different subsystems. Finally, the outputs from the previous two simulations were implemented in the GridLAB-D simulator to determine the power system transient response.

Three different cases were studied to analyze the efficacy of the proposed dynamic feedback system in improving microgrid restoration. The first case did not incorporate dynamic feedback, and it had the most aggressive restoration scheme. The second case included moderate dynamic feedback to improve the restoration. The third case included the strictest constraints for microgrid frequency, voltage, and current deviation for the most stable restoration scheme.

A.   Case 1: Restoration without dynamic feedback from power system simulation.

In the base case, service restoration was implemented without dynamic feedback from the power flow simulation. The optimization problem (1)-(33) was solved using GUROBI optimization software. The objective was to restore all the bus blocks in a minimum number of stages. The priorities of the bus blocks were assigned randomly. The switching sequence for this restoration scheme is shown in Figure 9. All of the bus blocks were restored in four stages.
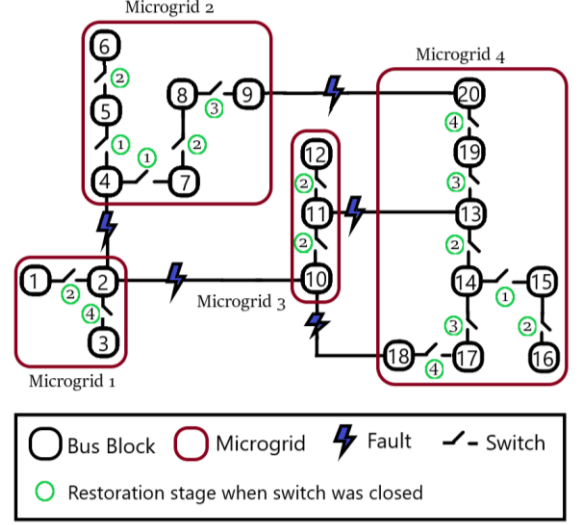

Figure 9: Restoration switching sequence for case 1.

The sequential load recovery sequence for each microgrid is shown in Figure 10. The load was restored in discrete steps due to the limited number of switches and ramping constraints of generators (21)-(22). This restoration sequence was very hasty as it tried to minimize the power outage time. The restoration solution was implemented in GridLAB-D power system simulator to analyze the severe effects of such an insensitive switching scheme.
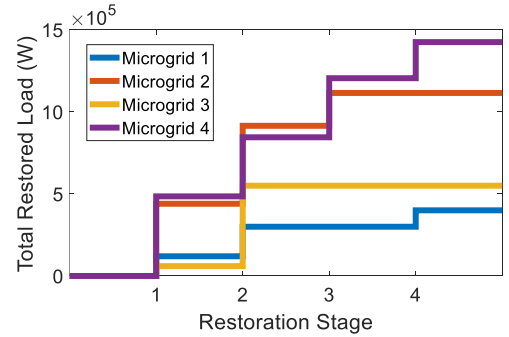

Figure 10: Case 1 optimized restoration without dynamic feedback.

After solving the MISOCP optimization problem, NS-3 communication system simulation was run to determine the delays in the transmission of information to different subsystems. This included the transmission of switching and control commands from the central controller to the microgrid controllers. The microgrid controllers distributed them to the generators, loads, and switches.

The control commands and communication delays were finally incorporated in the GridLAB-D power system simulation. This three-level simulation provided the cyber-physical implementation of the resilient distribution system.

The frequency and voltage of each node were monitored using phasor measurement units (PMUs). The phase current of each transmission line was also monitored using digital ammeters. The precision of these meters was one millisecond. Each microgrid controller aggregated the situational data for real-time monitoring of different subsystems.

When a bus block was switched on, all the loads and generators in that bus block were started. The power set-points of generators were dictated by the microgrid controllers. Unlike the optimization problem, three different types of loads were simulated in the GridLAB-D simulation: constant power loads, constant current loads and constant impedance loads. In this way, the power system simulation was intentionally made different from the optimization program. This was done to simulate the effect of load forecast errors on the power system restoration.

Huge voltage and frequency dips resulted from inductive load switching and power ramping. The frequency dips of the four black start diesel generators can be seen in Figure 11. Synchronous generators can be considered as the most dominant generators in an inverter-dominated microgrid. Therefore, these results give the effective frequency response of each microgrid. The diesel generators of microgrid 1 and microgrid 2 experienced the most severe frequency transients due to the presence of highly unbalanced loads on the three phases. The diesel generator of microgrid 3 was the most stable since this microgrid only had three phase lines with relatively balanced loads. Microgrid 4 was the largest in size hence it experienced transients in each stage from the remote switching of unbalanced loads.
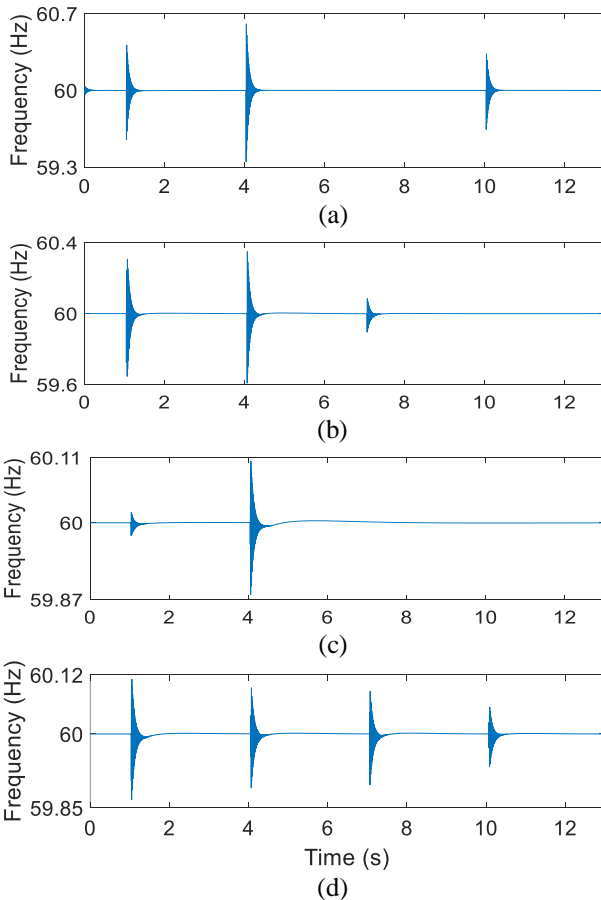

Figure 11: Frequency responses of diesel generators for four stages in case 1: (a) MG1 (b) MG2 (c) MG3 (d) MG4.

The terminal voltage of the black start diesel generator at node 76 can be seen in Figure 12. Huge voltage dips resulted from inductive load switching and power ramping. Unbalanced loading of the three phases caused the phase voltages to be effected greatly. The optimization problem could not predict the phase voltage spikes experienced in the simulation. These transient voltage spikes can cause commutation failure of IBDGs and trigger the power protection system.
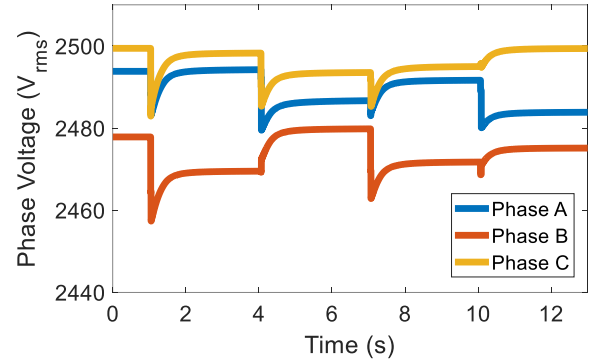

Figure 12: Phase voltages of node 76 for case 1.

The sequential switching of bus blocks also impacted the transmission line currents. The current spikes for line 76-77 can be seen in Figure 13. Unbalanced loading of generators caused the phase currents to be asymmetrical. Repetitive current spikes can cause overheating of generators, loads and lines.
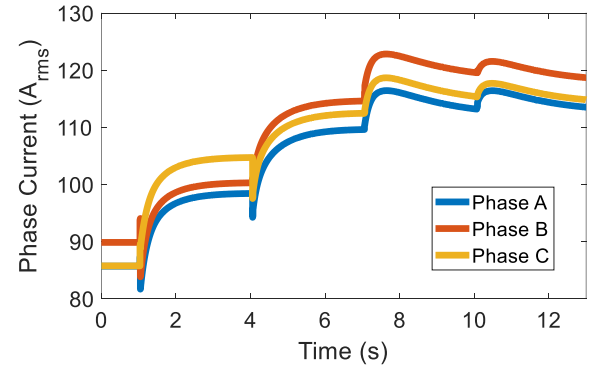

Figure 13: Phase currents of Line 76-77 for case 1.

The transient fault records prove that the simplified optimization model does not capture the complete picture of the power flow simulation. It is incapable of forecasting the transient response of synchronous generators, inverter-based generators, transmission lines, and loads. As a result, the optimized restoration solution resulted in severe voltage, current, and frequency spikes. These transients can damage sensitive electronic equipment and trigger the electrical protection system. This restoration scheme was the most aggressive as it did not include dynamic feedback from the GridLAB-D power system simulation.

Although complex optimization problems can accurately model the steady-state behavior of the power system elements, their transient behavior cannot be predicted. An active wide-area monitoring system was required to ensure safe operation during switching operations and power shuffling. The simulation was repeated to evaluate the effect of dynamic constraints (34)-(36) on the microgrid stability. The second and

third cases used real-time feedback from the power system simulation to improve the microgrid restoration.

B. Case 2: Moderate dynamic constraints (34)-(36) with $\Delta f^{max} = 0.25\ Hz, \Delta V^{max} = 120V, \Delta I^{max} = 10A$.

The second case used sequential dynamic feedback from the power system simulation to improve the restoration process. The restoration optimization problem (1)-(33) was solved to calculate the switching sequence for four stages. Then, NS-3 communication system simulation was run to determine the delays in the transmission of control commands to the different subsystems. The control commands and communication delays were finally incorporated in the GridLAB-D power system simulation.

The frequency and voltage of each node were monitored using PMUs. The phase current of each transmission line was also monitored using digital ammeters. The precision of these meters was one millisecond. Each microgrid controller aggregated the situational data for real-time monitoring of different subsystems.

After every restoration stage, each microgrid controller calculated the microgrid disturbance factor using (34) to quantify the violence experienced by it. This factor presented a summary of the entire microgrid after the restoration stage. It incorporated the effects of all voltage, current and frequency transients experienced by the loads, lines and generators. The microgrid disturbance factor was sent to the central controller for the next optimization stage.

The central controller used the feedback to restrain the recovery algorithm using (35)-(36). The decrease of maximum load recovery limit (36) gave the microgrid sufficient time to heal in the next stage.

After the power system simulation was completed for a particular stage, the restoration solution from that stage was retained, and the rest was discarded. Then, the optimization algorithm (1)-(33) was run again. The final switching sequence is shown in Figure 14. The restoration of all the bus blocks was completed in six stages.
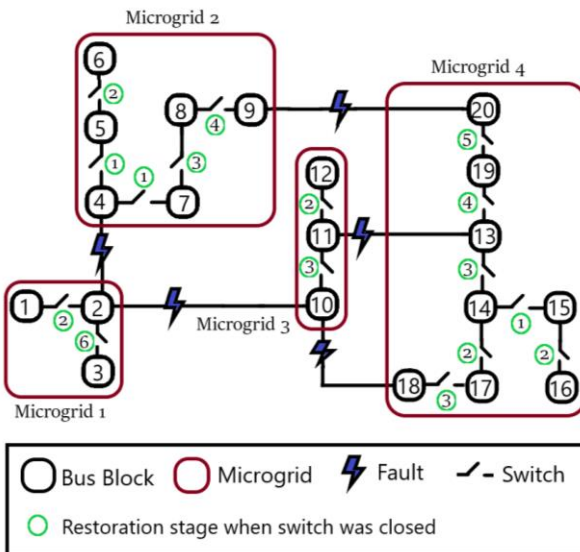

Figure 14: Restoration switching sequence for case 2.

Incorporating dynamic feedback (34)-(36) from the power system simulation made the rolling horizon sequential

restoration much slower. Each microgrid controller provided feedback about its current state to the central controller. The central controller was able to delay restoration of severely disturbed microgrids to allow more time to heal. This rolling horizon restoration scheme prevented repetitive transients from damaging the generators, loads and lines. Unlike the harsh switching scheme in case 1, this restoration scheme was more sensitive and safer.

The frequency of four black start diesel generators is plotted in Figure 15. The frequency dips were less severe compared to case 1, so the healing improved.

Microgrid 1 experienced a severe frequency transient in the second stage. The frequency of the diesel generator deviated by more than +/- 0.25 Hz. Hence further load restoration was delayed till the sixth stage.

Restoration of microgrid 2 was also much smoother. Repeated transients due to switching of multiple bus blocks at once were avoided.

Microgrid 3 was restored in three instead of two stages. Bus blocks were switched one by one. Hence, the peak frequency deviation was smaller. The feedback of microgrid controller delayed the load restoration. Hence, the healing of the microgrid was improved.

Microgrid 4 was restored in five instead of four stages. Severe frequency transients were avoided by restoring loads slowly. Multiple heavy loads were not restored in the same stage. This was only possible because of wide-area situational monitoring of the loads, lines and generators. The feedback from the disturbed subsystems enabled the central controller to improve restoration of the microgrid.
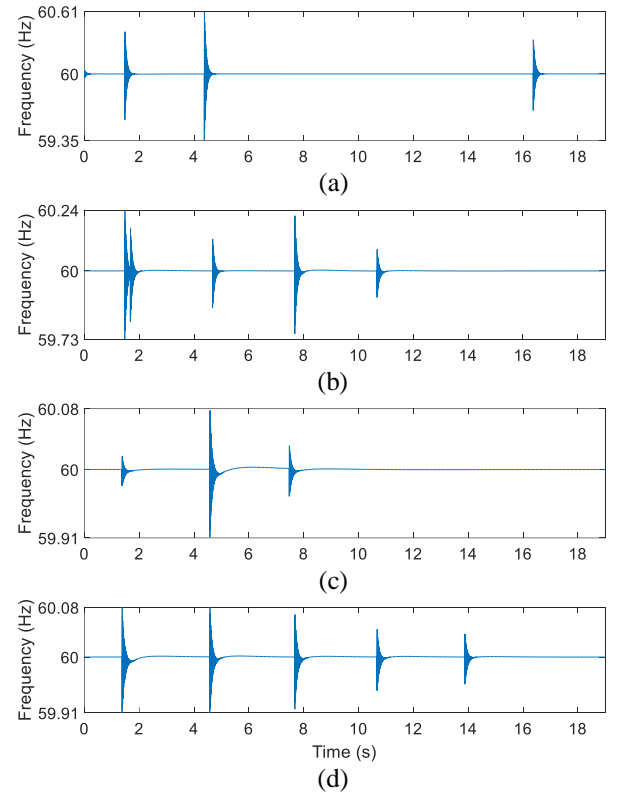

Figure 15: Frequency of four diesel generators for case 2: (a) MG1 (b) MG2 (c) MG3 (d) MG4.

C. Case 3: Strict dynamic constraints (34)-(36) with $\Delta f^{max} = 0.10\,Hz, \Delta V^{max} = 60V, \Delta I^{max} = 5A$.

The third case imposed the strictest constraints on the microgrid voltage, current, and frequency deviation to ensure a smooth restoration for each microgrid. After every restoration stage, each microgrid controller calculated the microgrid disturbance factor to summarize the state of the entire microgrid. The microgrid disturbance factor was sent to the central controller for the next optimization stage.

The central controller used the feedback to restrain the recovery algorithm to allow more time for the microgrid healing process. The final switching sequence is shown in Figure 16. The restoration was completed in seven stages.

The immediate effect of introducing strong dynamic feedback was that restoration of microgrid 1, 2 and 4 was completely stopped in the second stage. The initial transients of first stage greatly disturbed the microgrids. Hence the microgrid controllers informed the central controller about the critical condition. The central controller was able to delay restoration of severely disturbed microgrids to allow more time to heal. This rolling horizon restoration scheme prevented repetitive transients from damaging the generators, loads and lines.

The microgrids were able to heal in stage 2. Hence, the microgrid disturbance factors (34) were small for this stage. This allowed the load restoration limits (35)-(36) to increase for the following stages. The dynamic constraints were very strict. Hence, the restoration algorithm prevented simultaneous switching of heavy loads. Overall, the restoration of microgrids was greatly improved by taking feedback from the disturbed IEDs.
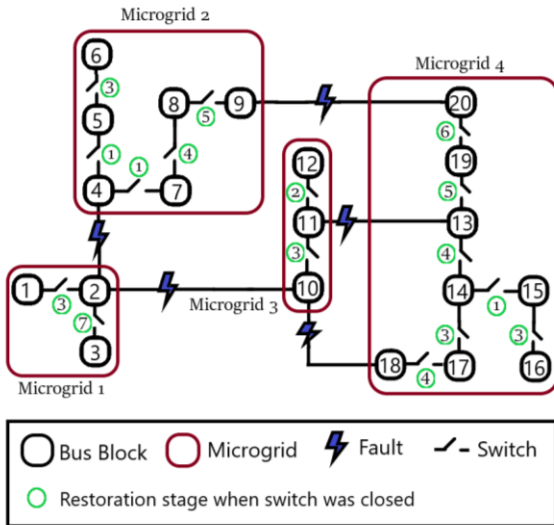

Figure 11: Restoration switching sequence for case 3.

As seen in Figure 17, the frequency of the microgrids was more stable compared to cases 1 and 2. The frequency oscillations were short-lived because the switching of bus blocks was less frequent. Hence, the restoration became much safer by making the dynamic constraints very strict.
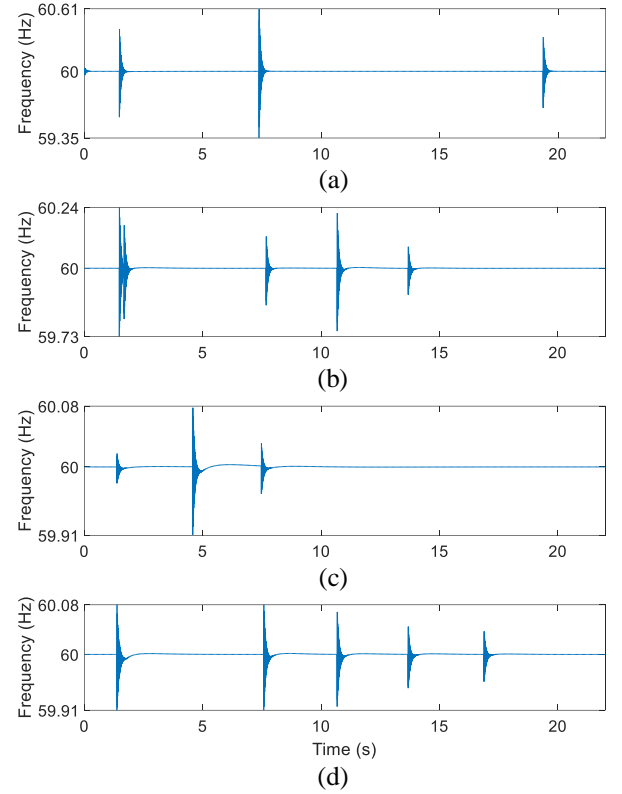

Figure 12: Frequency of diesel generators for case 3: (a) MG1 (b) MG2 (c) MG3 (d) MG4.

VII. DISCUSSION

Smart grid restoration was carried out for three different cases. The first case did not use dynamic feedback from power system simulation. Hence, the restoration was very fast and aggressive. The switching of bus blocks resulted in long-lasting frequency, voltage, and current oscillations. These oscillations could not be predicted by the optimization problem. Therefore, the restoration had to be improved.

The second case used dynamic feedback from the power flow simulation to restrain the restoration algorithm after every stage. Based on the value of the microgrid disturbance factor, the microgrid restoration was delayed. The final restoration was much smoother than the base case, and the microgrids got a longer time to heal from the transients.

In the third case, the strictest constraints for frequency, voltage, and current deviation were imposed. The transient nodal voltage constraints, nodal frequency constraints, and line current constraints reinforced the dynamic stability of the healing microgrid. As a result, the restoration took more stages, and the microgrids got a much longer time to heal from the transients. The frequency oscillations were short-lived because the switching of bus blocks was less frequent.

The maximum load restoration limits are compared in Figure 18. Initially all three cases had the same restoration limit. Hence, the stage 1 switching sequence of bus blocks was the same in cases 1, 2 and 3.

In case 1, the maximum restoration limit of each stage was the same because dynamic constraints were not imposed. Dynamic response of microgrids was not considered in case 1. Hence the load restoration limit increased steadily in each stage. This restoration scheme was the most aggressive for the loads, lines and generators.
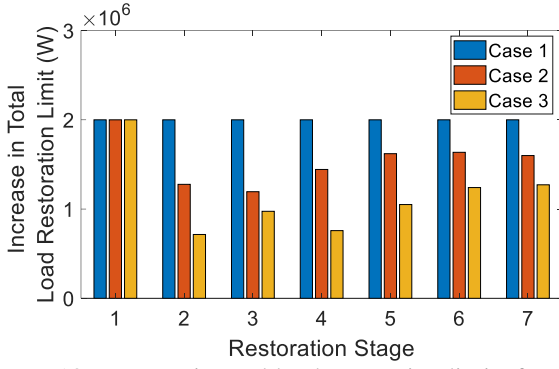
Figure 13: Increase in total load restoration limits for each restoration stage.

Case 2 restoration was much smoother because moderate dynamic feedback was used in the rolling horizon optimization model. The central controller was able to modulate load restoration limit (35)-(36) of the microgrids based on their dynamic feedback (34). The load restoration limit increased slowly hence the restoration was much slower. The maximum restoration limit dropped after the first stage because the dynamic constraints were violated. This delayed the subsequent restoration. Eventually, the microgrids became stable, and the maximum load restoration limit started to increase.

A similar trend was seen for case 3. The dynamic constraints were the strictest in this case. The load restoration limit increased very slowly because of the strong feedback of disturbed microgrids. The microgrids became stable after four restoration stages. Then, the maximum load restoration limit started to increase.

The summary of the restored bus blocks for the three cases is given in Table 1.

Table 1. Summary of load restoration in three cases.

| Restoration Stage | Restored bus blocks | | |
	Case 1	Case 2	Case 3
1	MG1: 2 MG2: 4, 5, 7 MG3: 11 MG4: 14, 15	MG1: 2 MG2: 4, 5, 7 MG3: 11 MG4: 14, 15	MG1: 2 MG2: 4, 5, 7 MG3: 11 MG4: 14, 15
2	MG1: 1 MG2: 6, 8 MG3: 10, 12 MG4: 13, 16	MG1: 1 MG2: 6 MG3: 12 MG4: 16, 17	MG3: 12
3	MG2: 9 MG4: 17, 19	MG2: 8 MG3: 10 MG4: 13, 18	MG1: 1 MG2: 6 MG3: 10 MG4: 16, 17
4	MG1: 3 MG4: 18, 20	MG2: 9 MG4: 19	MG2: 8 MG4: 13, 18
5	-	MG4: 20	MG2: 9 MG4: 19
6	-	MG1: 3	MG4: 20
7	-	-	MG1: 3

The final load restoration for the three cases is compared in Figure 19. Complete recovery took four stages in case 1, six stages in case 2, and seven stages in case 3. By avoiding simultaneous switching of heavy loads, the transient response of the microgrids was improved. This proves that the dynamic

feedback based on wide-area situational monitoring made the restoration smoother and improved the dynamic stability of all four microgrids.
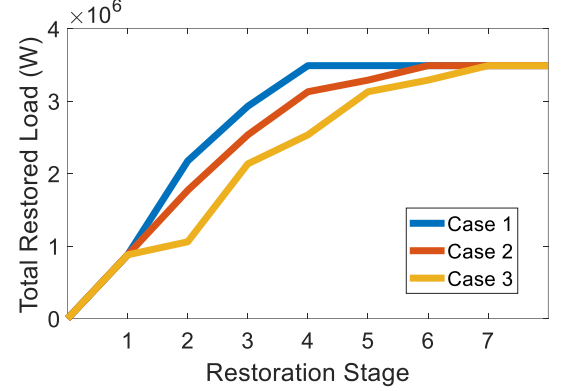

Figure 19: Comparison of load restoration in three cases.

The pervasive communication system enabled continuous scanning of operational data for greater control and flexibility. However, the extensive monitoring required enhanced communication channel utilization. The repeated synchronization also introduced substantial computation overhead.

VIII. CONCLUSION

This research demonstrated a cyber-physical implementation of a resilient distribution system. The switching sequence and the load restoration decisions determined by solving the MISOCP optimization problem were implemented over a distributed control framework. The different subsystems operated cooperatively with two-way negotiations to exchange information and control signals across the network. Based on the communication requirements, network traffic was simulated in NS-3 to determine the latencies of the data transmission. The resulting reconfiguration commands and inter-switch operating delays were finally simulated in GridLAB-D to determine the transient response. Microgrid controllers used the measurements of distributed IEDs to quantify the damage afflicted on the loads, lines and generators. This transient response provided feedback for the next stage of the rolling horizon restoration optimization problem. By imposing strict dynamic constraints, the microgrid restoration was delayed to allow microgrids to heal from transients. In effect, the dynamic feedback based on wide-area situational monitoring improved the restoration of inverter-dominated microgrids.

REFERENCES

[1] Z. Wang and J. Wang, "Self-healing resilient distribution systems based on sectionalization into microgrids", IEEE Transactions on Power Systems, vol. 30, no. 6, pp. 3139-3149, Nov. 2015.

[2] A. Arif and Z. Wang, "Networked microgrids for service restoration in resilient distribution systems", IET Generation, Transmission and Distribution, vol. 11, no. 14, pp. 3612-3619, September 2017.

[3] L. Che and M. Shahidehpour, "Adaptive formation of microgrids with mobile emergency resources for critical service restoration in extreme conditions", IEEE

Transactions on Power Systems, vol. 34, no. 1, pp. 742-753, Jan. 2019.

[4] A. Arif, B. Cui and Z. Wang, "Switching device-cognizant sequential distribution system restoration", IEEE Transactions on Power Systems, vol. 37, no. 1, pp. 317-329, Jan. 2022.

[5] Y. Xu, C. -C. Liu, K. P. Schneider, F. K. Tuffner and D. T. Ton, "Microgrids for service restoration to critical load in a resilient distribution system", IEEE Transactions on Smart Grid, vol. 9, no. 1, pp. 426-437, Jan. 2018.

[6] B. Chen, Z. Ye, C. Chen and J. Wang, "Toward a MILP modeling framework for distribution system restoration", IEEE Transactions on Power Systems, vol. 34, no. 3, pp. 1749-1760, May 2019.

[7] C. Chen, J. Wang, F. Qiu and D. Zhao, "Resilient distribution system by microgrids formation after natural disasters", IEEE Transactions on Smart Grid, vol. 7, no. 2, pp. 958-966, March 2016.

[8] Q. Zhang, Z. Ma, Y. Zhu and Z. Wang, "A two-level simulation-assisted sequential distribution system restoration model with frequency dynamics constraints", IEEE Transactions on Smart Grid, vol. 12, no. 5, pp. 3835-3846, Sept. 2021.

[9] Y. Du, X. Lu, J. Wang and S. Lukic, "Distributed secondary control strategy for microgrid operation with dynamic boundaries", IEEE Transactions on Smart Grid, vol. 10, no. 5, pp. 5269-5282, Sept. 2019.

[10] Y. Wen, W. Li, G. Huang and X. Liu, "Frequency dynamics constrained unit commitment with battery energy storage", IEEE Transactions on Power Systems, vol. 31, no. 6, pp. 5115-5125, Nov. 2016.

[11] B. Chen, C. Chen, J. Wang and K. L. Butler-Purry, "Sequential service restoration for unbalanced distribution systems and microgrids", IEEE Transactions on Power Systems, vol. 33, no. 2, pp. 1507-1520, March 2018.

[12] O. Bassey, K. L. Butler-Purry and B. Chen, "Dynamic modeling of sequential service restoration in islanded single master microgrids", IEEE Transactions on Power Systems, vol. 35, no. 1, pp. 202-214, Jan. 2020.

[13] B. Chen, C. Chen, J. Wang and K. L. Butler-Purry, "Multi-time step service restoration for advanced distribution systems and microgrids", IEEE Transactions on Smart Grid, vol. 9, no. 6, pp. 6793-6805, Nov. 2018.

[14] J. Zhao, H. Wang, Y. Liu, Q. Wu, Z. Wang and Y. Liu, "Coordinated restoration of transmission and distribution system using decentralized scheme", IEEE Transactions on Power Systems, vol. 34, no. 5, pp. 3428-3442, Sept. 2019.

[15] J. Zhao, H. Wang, Y. Hou, Q. Wu, N. Hatziargyriou, W. Zhang and Y. Liu, "Robust distributed coordination of parallel restored subsystems in wind power penetrated transmission system", IEEE Transactions on Power Systems, vol. 35, no. 4, pp. 3213-3223, July 2021.

[16] H. Gu, R. Yan, T. K. Saha, E. Muljadi, J. Tan and Y. Zhang, "Zonal inertia constrained generator dispatch considering load frequency relief", IEEE Transactions on Power Systems, vol. 35, no. 4, pp. 3065-3077, July 2020.

[17] J. Li, X. Ma, C. Liu and K. P. Schneider, "Distribution system restoration with microgrids using spanning tree search", IEEE Transactions on Power Systems, vol. 29, no. 6, pp. 3021-3029, Nov. 2014.

[18] J. Zhao, Q. Wu, N. D. Hatziargyriou, F. Li and F. Teng, "Decentralized data-driven load restoration in coupled transmission and distribution system with wind power", IEEE Transactions on Power Systems, vol. 36, no. 5, pp. 4435-4444, Sept. 2021.

[19] C. Wang, S. Lei, P. Ju, C. Chen, C. Peng and Y. Hou, "MDP-based distribution network reconfiguration with renewable distributed generation: Approximate dynamic programming approach", IEEE Transactions on Smart Grid, vol. 11, no. 4, pp. 3620-3631, July 2020.

[20] M. R. Dorostkar-Ghamsari, M. Fotuhi-Firuzabad, M. Lehtonen and A. Safdarian, "Value of distribution network reconfiguration in presence of renewable energy resources", IEEE Transactions on Power Systems, vol. 31, no. 3, pp. 1879-1888, May 2016.

[21] W. Sun, S. Ma, I. Alvarez-Fernandez, R. Nejad, A. Golshani, "Optimal self-healing strategy for microgrid islanding", IET Smart Grid, vol. 1, no. 4, pp. 143– 150, 2018.

[22] D. P. Chassin, K. Schneider and C. Gerkensmeyer, "GridLAB-D: An open-source power systems modeling and simulation environment", 2008 IEEE/PES Transmission and Distribution Conference and Exposition, pp. 1-5, 2008.

[23] 123-Bus Feeder. [Online]. Available: https://site.ieee.org/pes-testfeeders/resources.

[24] J. Farooq and T. Turletti, "An IEEE 802.16 WiMAX module for the ns-3 simulator", Proceedings of the 2nd International Conference on Simulation Tools and Techniques, pp. 1-11, 2009.